Coastal Dynamics 2017
Paper No. 011

INCIPIENT MOTION OF SAND-OIL AGGLOMERATES

Melanie M.A. Schippers[1], Niels G. Jacobsen[1], P. Soupy Dalyander[2], Timothy Nelson[2], Robert McCall[1]

Abstract

A newly developed computational fluid dynamics model applicable to objects partly buried in a sand bed is used to predict the incipient motion of sand-oil agglomerates (SOAs). The model is applied for both 2D and 3D cases. The force coefficients describing the forces on the SOAs were compared with theoretical and experimental data. The model predicted the force coefficients accurately for both types of data. It is found that the critical mobility number for incipient motion of SOAs depends on the Keulegan-Carpenter number and to a lesser extent the Reynolds number. Spherical SOAs are most likely to rotate (while unburied), while flat SOAs are most likely to slide. Nonetheless, the large number of parameters, needed to describe of this environmental problem, introduces several uncertainties originating from the formation process of SOAs in the field. The uncertainties relate to density, dimensions, and shape of the SOA. Therefore, the results suggest that the evaluation of the incipient motion of SOAs should be approached probabilistically rather than deterministically.

Key words: sand-oil agglomerates, incipient motion, numerical modeling

1. Introduction

The oil spilled from Deep Water Horizon in the Gulf of Mexico in 2010 migrated to sandy shorelines and re-oiling of the beaches is a recurring problem to this day. Re-oiling occurs in the form of sand-oil agglomerates (SOAs) that are heavier than water with a density between 1800-2400 kg/m3 (Dalyander et al., 2015a). The agglomerates initially formed as oil mixed with suspended sediment and settled to the seabed where it formed mats tens of meters long. The mats subsequently broke into smaller cm-sized spherical or disc agglomerates.

SOAs are much larger than the surrounding sediment, which makes the incipient motion and subsequent transport different from classical sediment dynamics formulations often developed for uniform grain-sized beds. Dalyander et al. (2014) studied the expected mobility and transport patterns of SOAs using shear-stress based thresholds of motion and a hydrodynamic model to evaluate flow direction and magnitude under a broad range of wave conditions. They found that mobility occurred primarily during storms and that SOAs could concentrate within inlets and where there were alongshore transport convergences and they identified uncertainties in the driving forces and thresholds of incipient motion.

In Dalyander et al. (2015a), the physical dynamics of sand and oil agglomerates were studied by analyzing the behavior of artificial SOAs in the nearshore. The observations compared best with a shear-stress formulation where the hydraulic roughness was related to the size of the SOA and not the surrounding sand, but uncertainties in predicting the mobility of cm-sized particles were indicated. Burial was observed for, immobile artificial SOAs with diameters of 5.0-10 cm.

Observations of Terrile et al. (2006) of the mobility of coarse particles under shoaling waves indicated that a combination of shear stress and pressure gradient initiates motion. This was also observed by Frank et al. (2015) in a study of the onset of motion of gravel-sized sediment. The contribution of the shear stress relative to the contribution of the pressure gradient was related to the length of the orbital excursion: for

[1] Deltares, Boussinesqweg 1, 2629HV Delft, The Netherlands (niels.jacobsen@deltares.nl)
[2] U.S. Geological Survey, 600 Fourth Street South, St. Petersburg, FL 33701, U.S. (sdalyander@usgs.gov)

small orbital excursions, the contribution of the pressure gradient dominated, whereas for long orbital excursions, shear stress was more dominant.

The fundamental assumption in this work is that the forces acting on an object on the seabed can be described with the Morison equation (e.g. Sumer and Fredsøe, 1999), i.e. the time history of the forces can be constructed based on the knowledge of the free stream velocity field, the dimensions of the object and associated force coefficients. The force coefficients are the drag coefficient (C_D), the added mass coefficient (C_M) and the lift coefficient (C_L). The use of the Morison equation allows for a total inline force which changes gradually from acceleration dominated forcing (added mass) to velocity dominated forcing (drag) with an increasing Keulegan–Carpenter (KC) number.

Late in this work it was observed that the lift force is poorly described by the Morison formulation (see Eq. 9), since the maximum lift force is not observed during at the instant of maximum velocity, but rather at the time of maximum acceleration of the fluid. This led to a renewed investigation of literature, and it was found that already Jacobsen et al. (1988) and Bryndum et al. (1992) observed a poor fit between the Morison equation and a pipeline resting on the seabed; see in particular the plotted time series in Jacobsen et al. (1988). Nonetheless, application of the Morison is still frequently encountered in literature on forces acting on bottom-mounted objects (An et al., 2011).

From simple force and moment equilibriums, it was found that the incipient motion of an object on the seabed is described by a mobility number:

$$\Psi_{cr} = \frac{u_m^2}{(s-1)gD} \tag{1}$$

Here, Ψ_{cr} is the critical mobility number, u_m is the amplitude of the orbital velocity, s is the relative density of the object, g is the acceleration due to gravity and D is a characteristic length scale. The full analysis for a circular and a square object is found in Schippers (2017) for a laterally averaged, two-dimensional (2DV) situation.

The present work addresses the incipient motion of SOAs (and other objects much larger than the surrounding sediment) with the aid of detailed Computational Fluid Dynamics (CFD) modeling used to evaluate the force acting on SOAs. The predictions of incipient motion are compared to laboratory experiments where behavior of artificial SOAs was observed. The results from this work will facilitate better estimates for practical engineering models and the work will also provide insight into the type of instability for large objects (sliding or rotation of the object).

2. Mathematical Framework

The mathematical approach is that of the multi-purpose CFD framework OpenFoam (Weller et al., 1998; version foam-extend-3.1). Since SOAs can become buried, it is important to capture the hydrodynamic forces on the SOAs from within the sand bed, such that the effect of burial on the incipient motion can be described. No mathematical model describing both the fluid flow and the Darcy flow was available, so a custom solver consisting of two computational meshes (one for the fluid and the other for the seabed) was implemented. This approach was adopted over the use of flow resistance of the sand in a single computational grid, since it allowed the use of existing turbulence models in the fluid region. The pressure on the object is also determined in the sand (Figure 1) indicating that the pressure distribution in the sand is important for the resulting force on the object.

This type of mathematical modeling has previously been performed for pipelines (An et al., 2011) to study the hydrodynamic loads on a partly buried pipeline in 2DV. To the authors' knowledge, the present work is the first that achieves the modeling of the flow in both sand and fluid for a generalized three-dimensional model.

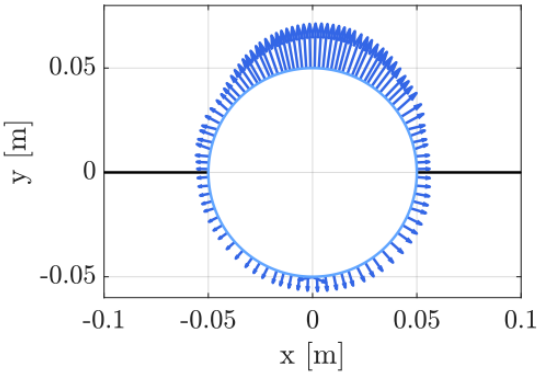

Figure 1: An example of the distribution of the total pressure round a 2DV sphere half-buried in sand. Sand for $y < 0$.

2.1. *Solution to the flow in the fluid region*

The hydrodynamics in the fluid region is described by the incompressible continuity equation:

$$\nabla \cdot \mathbf{u} = 0 \tag{2}$$

together with the Reynolds averaged Navier-Stokes equations:

$$\frac{\partial \mathbf{u}}{\partial t} + \nabla \cdot \mathbf{u}\mathbf{u}^T = \frac{1}{\rho}\nabla p + \nabla \cdot (\nu + \nu_T)\nabla \mathbf{u} \tag{3}$$

Here, $\boldsymbol{u}$ is the velocity vector, t is time, ρ is the density, p the total pressure, ν the kinematic molecular viscosity and ν_T the eddy viscosity. Superscript T is the transpose of the velocity vector. The eddy viscosity is calculated with the $k-\omega$ SST turbulence closure (Wilcox, 2006).

The computational domain is periodic in the x-direction, so the only required boundary conditions are on the top, the bottom, the lateral sides (for 3D simulations), and the SOA. The top and lateral sides are treated with a slip boundary and the bottom and SOAs as no-slip. Note that there is no external, driving body force in Eq. (3); the driving force is discussed in Section 2.3.

2.2. *Solution to the flow in the sand region*

The momentum equation in the seabed is derived following a number of assumptions: (i) the added mass due to acceleration of the fluid is small, (ii) the flow resistance can be described by a Darcy term thus neglecting the Forchheimer resistance, and (iii) all convective terms are negligible. Based on these assumptions, the momentum equation becomes:

$$\frac{\partial \mathbf{u}}{\partial t} = -\frac{1}{\rho}\nabla p - a\mathbf{u} \tag{4}$$

where a is the Darcy resistance term modeled according to Van Gent (1995). Applying the continuity equation in Eq. (2) to Eq. (4) it is found that the solution to the pressure in the sand follows the Laplace equation:

$$\nabla^2 p = 0 \tag{5}$$

This is the primary equation to be solved in the sand, since there is no coupling issue between velocity and pressure in the sand due to the linearity of the momentum equation. The transient velocity field in the sand can be derived by simple substitution of p into Eq. (4) at the end of a time step. The linearity of Eqs. (4) and (5) limits the use of the model to Darcy-type flow, e.g. gravel-beds cannot be captured accurately.

2.3. *Forcing of the fluid flow and coupling of the computational meshes*

A standard approach to force a flow on a periodic grid is to apply an internal body force in every single computational cell. This is a working solution, but care has to be taken at solid boundaries that are not oriented perpendicular to the direction of the body force. The reason is that a Neumann boundary condition for the pressure together with the normal component of the body force prescribes acceleration across the solid boundary. This is inconsistent with the physical system and tests with the model have shown that the iterative solver converges slower towards some pressure solution (not shown here).

The chosen approach is to enforce a constant jump in the pressure across the cyclic boundary, while the pressure varies linearly along the computational domain. This approach is similar to the physical system of a U-tube (Jensen et al., 1989). Normally, the pressure jump, Δp, is prescribed based on the continuous description of the pressure gradient as follows:

$$\Delta p = \lambda \frac{\partial p}{\partial x} = -\rho \lambda \frac{\partial u_0}{\partial t} \tag{6}$$

λ is the length of the computational domain and u_0 is the free-stream velocity. This approach is not feasible for the present type of application, where the computational time step varies with a prescribed Courant criterion. The reason is that $\overline{\Delta p}$ (the time-averaged pressure gradient) does not vanish for long simulations due to temporal discretization errors. The consequence is that there is a numerically induced mean force in the system due to accumulated contributions from an inaccurate treatment of the forcing. To resolve this issue, the pressure jump is determined in an integral fashion:

$$\Delta p = -\rho \frac{\lambda}{\Delta t} \int_{t_0}^{t_0+\Delta t} \frac{\partial u_0}{\partial t} \mathrm{d}t \tag{7}$$

The difference between Eq. (6) and Eq. (7) is that the latter vanishes when averaged over a sufficiently long time and there is no numerically induced mean loading on the system. Practical testing has shown that this method is robust and has a reduced computational cost in comparison with the use of a body force.

Δp is assigned to both the fluid and sand regions and Δp is also kept constant over the height of the computational domain. This approach essentially assumes that the dimensions of the SOA are much smaller than the wavelength, which is a valid assumption, since the largest SOAs used in this work are 10 cm in diameter.

The two computational meshes are coupled in a segregated manner: The solution is found in the sand first and secondly in the fluid with an update of matching boundaries between the two solution steps. The pressure solution from the fluid region is mapped to the boundary for the sand region and the velocity field in the sand region is mapped to the boundary condition for the fluid region. The meshing of the two neighboring boundaries does not have to be matching, while a second order accurate linear interpolation is adopted to map the physical properties. The interpolation stencil is based on a least-square interpolation routine. This higher order interpolation scheme is adopted to prevent wiggles in the numerical solution.

3. Validation

3.1 Validation against Yamamoto et *al.* (1974)

Yamamoto et al. (1974) presented a theoretical solution to the lift and added mass coefficient around a pipeline (a circle in the 2DV plane) as a function of the distance from the pipeline to the adjacent wall. The case of a pipeline suspended above the bed is not relevant for the present work; nonetheless the results by Yamamoto et al. (1974) serve as a good validation case for the numerical force coefficients. The force coefficients are evaluated with a least-squares technique to fit the simulated force on the SOA to the Morison equation (as in Sumer and Fredsøe, 1999):

$$F_D = \frac{1}{2}\rho D C_D \,|u|\,u + \rho C_M A \frac{\partial u}{\partial t} \tag{8}$$

and

$$F_L = \frac{1}{2}\rho C_L D u^2 \tag{9}$$

Here, F_D is the drag force, D is the diameter of the pipeline, C_D is the drag coefficient, C_M is the added mass coefficient, A is the cross-sectional area of the pipeline, F_L is the lift force and C_L is associated lift coefficient. The free stream velocity, u, is used for all positions of the object, i.e. also when the object is partly or completely buried in the sand. The seabed was simulated to consist of a median grain diameter of 0.25 mm and to have a porosity of 0.4.

Numerical simulations were performed with a pipeline at several distances away from the bed in the range $e/D \in [-2, 2]$, where e is the signed distance from the lowest point of the pipeline to the sand bed, i.e. the pipeline is resting on the sand bed for $e/D = 0$ and is precisely buried in the sand bed for $e/D = -1$. The Keulegan-Carpenter number was set to $KC = u_m T/D = 1$ for all simulations to conform to the assumptions in the theory of Yamamoto et al. (1974). T is the wave period.

The results for the added mass coefficient and the lift coefficient are depicted in Figures 2 and 3 together with the analytical expression by Yamamoto et al. (1974). The numerical prediction for positive values of e/D is close to the analytical expression. The benefit of the numerical model is that it is possible to extend the solution into the bed, which was not covered by the analytical model.

Jacobsen et al. (1989) performed an experimental investigation of the forces on partly buried pipelines in an oscillatory flow. The pipeline was placed on a solid bed, so the 'burial' was achieved by removing a part of the cylinder. This means that the results by Jacobsen et al. (1989) essentially only consider the fluid forces in the water and not in both water and sand. The fluid part of the hydrodynamic load is used to compare with Jacobsen et al. (1989) and these results are also included in Figures 2 and 3. This shows that the model is capable of predicting the loads on the object. The results furthermore show that there is a significant difference in C_M, when the pressure in the sand is included or not. This highlights the necessity of considering the processes in the sand.

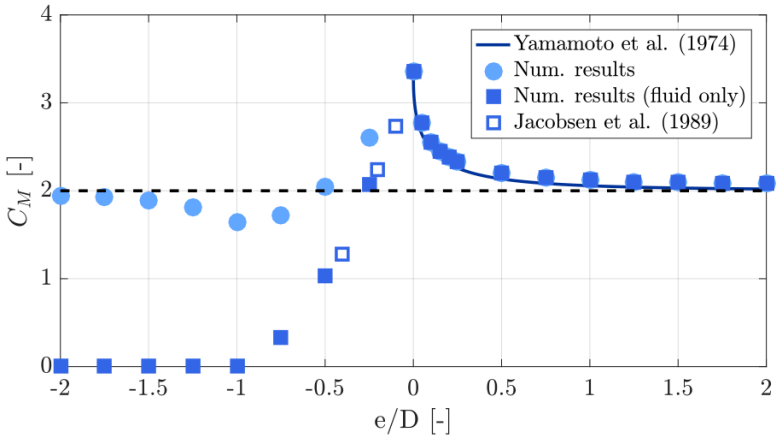

Figure 2: Validation of the added mass coefficient, C_M. The experimental data by Jacobsen et *al.* (1989) were only obtained in the fluid region.

The lift coefficient decreases and becomes 0 for $e/D = -1$, when the pipeline is buried (Figures 2 and 3), which makes intuitive sense. The behaviour of C_M, however, is completely different and somewhat surprising since $C_M = 2$ for deep burial ($e/D < -2$) and C_M is based on the accelerations in the free stream. The value of $C_M = 2$ for deep burial ($e/D \ll 1$) is obtained, because the same pressure gradient is used to drive the flow in the sand and in the fluid.

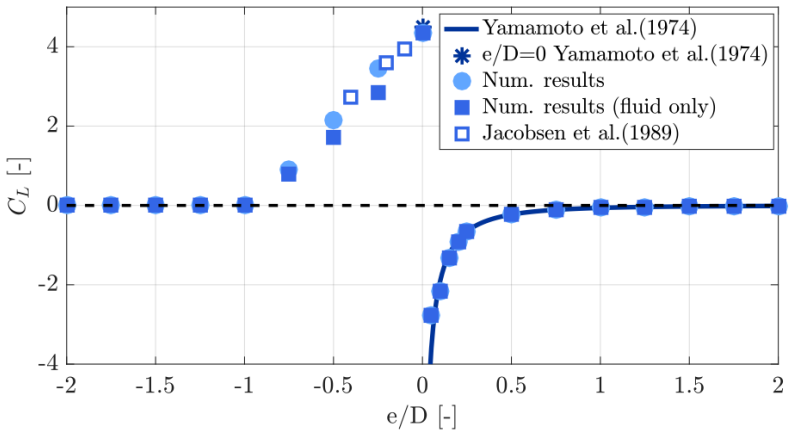

Figure 3: Validation of the lift coefficient, C_L. The experimental data by Jacobsen et *al.* (1989) were only obtained in the fluid region.

The explanation relates to the origin of the pressure field around a circular cylinder in a homogenous, porous medium. The classical solution to the added mass coefficient for a free cylinder is summarized in Sumer and Fredsøe (1999), where they show that C_M follows from the insertion of the potential flow solution around a cylinder into the Bernoulli equation. The same potential flow solution (with a different amplitude of the velocity potential) holds for a circle in a porous medium. The Bernoulli equation, however, is no longer energy conserving due to the presence of a resistance term from the porous medium: $a\phi$, in which ϕ is the velocity potential and a the resistance coefficient. The term $a\phi$ essentially describes the pressure drop along a streamline and the presence of $a\phi$ leads to an additional pressure field around the cylinder. This pressure field compensates for the smaller velocities in the porous medium and one reach the result that $C_M = 2$ for deep burial.

The added mass also equals 2 when the cylinder is half buried ($e/D = -0.5$). The situation is explained by applying potential theory, since the sea bed is placed perfectly along the symmetry line, where there is no interaction between the solution in the water and the sand, respectively. Therefore, each half of the cylinder experiences the same potential flow solution as in the case of a free or deeply buried cylinder. (The slight deviation of $C_M = 2$ for $e/D = -0.5$ is attributed to viscous effects in the fluid region).

3.2 Validation against Bryndum (1992)

The validation in Section 3.1 is valid only for small KC and small Reynolds numbers. To investigate conditions for high KC and high Reynolds numbers in the free-stream the experimental data by Bryndum et al. (1992) is used. They oscillated a bottom mounted cylinder back and forth and evaluated force coefficients based on the least-squares approach. The experiment was conducted for different KC numbers and different values of the surface roughness of the cylinder. The numerical results have been compared with the experimental data of Bryndum et al. (1992) as presented in Sumer and Fredsøe (1999).

Several values of the diameter of the circular cross section placed on the seabed were evaluated numerically and resulted in values of the surface roughness between the fine and rough conditions investigated by Bryndum et al. (1992). The comparison with the drag coefficient is satisfactory and within 10-15% of experimental (Figure 4), though it is difficult to quantity, as Bryndum et al. (1992) only reported lines of best fit.. The lift coefficient is somewhat under-estimated (Figure 5), even though the same fitting approach to the Morison equation was applied. No explanation for this under-estimation was found.

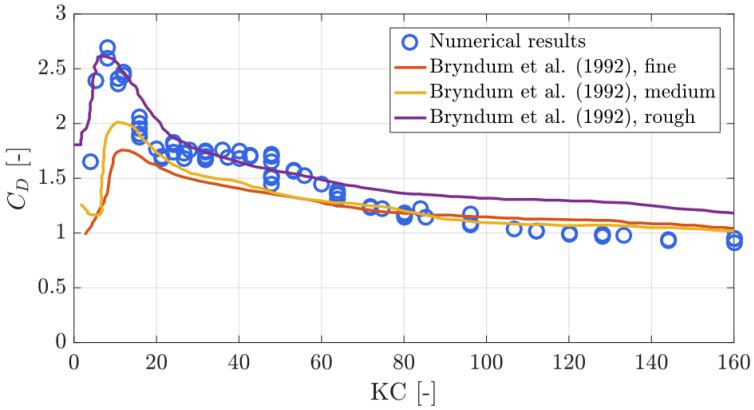

Figure 4: The drag coefficient evaluated with a least-squares fit to the Morison equation. The lines are experimental data by Bryndum et *al.* (1992) and the markers the present numerical results.

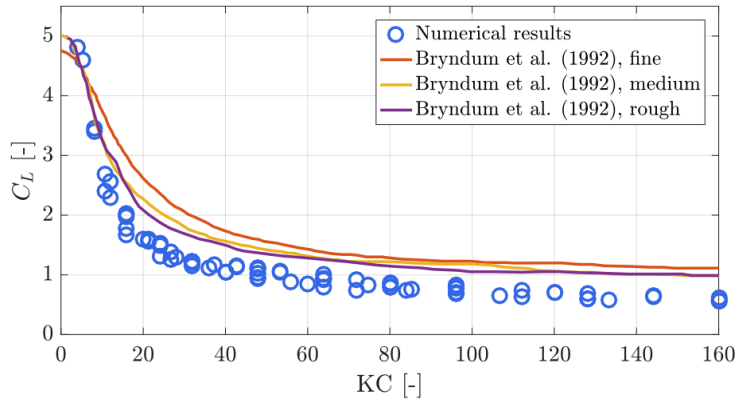

Figure 5: The lift coefficient evaluated with a least-squares fit to Eq. 9. The lines are experimental data by Bryndum et *al.* (1992) and the markers the present numerical results.

4. Results

In the work by Schippers (2017), the stability of both a circular and a box shaped object was analyzed and considered as representative shapes for SOAs in 2DV simulations. In this work, only results for the circular shaped object are presented. The results are presented for both an unburied condition and the buried condition. In all simulations, the bed was kept flat and no sediment transport of the surrounding sand was considered.

4.1 Summary of Experiments

Observed incipient motion data were obtained using artificial sand-oil agglomerates (aSOAs) that were constructed of natural sand and wax. These aSOAs range in size from 0.5-10 centimeters in diameter and include both spherical and ellipsoidal shapes (Dalyander et al., 2015b). The aSOAs were deployed in March, 2014 in the Sediment Dynamics Laboratory's Small-Oscillatory Flow Tunnel (S-OFT) located at the Naval Research Laboratory in Stennis Space Center, Mississippi. Asymmetric oscillatory flow were driven in the tank with a flywheel at variable frequency (20-90 rpm) and stroke length (22, 33, or 44 cm). During the experiments providing the data presented below, the aSOAs were deployed on a flat, roughened floor, with incipient motion detected through visual inspection of images from high-definition Digital-SLR cameras. Velocities in the tank were measured with a Vectrino acoustic velocity profiler mounted in the center of the tank.

4.2 Predictions of the critical mobility number

The simulations used to predict the force acting on a circular pipeline are already presented in Figures 4 and 5 for a pipeline resting on top of the bed (unburied condition). Similar plots are presented for various degrees of burial in Schippers (2017). Force coefficients are derived from the numerical simulations to form a lookup table including wave periods, orbital velocity amplitudes, and geometric SOA properties, so that a limited number of CFD computations is required. Subsequently, it is possible to evaluate the critical mobility number by prescribing the density of the SOA.

The incipient motion is evaluated for both sliding and rotating motion, so a parameterization of the resulting distance from the force to the point of rotation (the arm) was derived. The parameterization of the arm was found to be surprisingly independent on KC numbers, i.e. practically constant over the parameter set. The reader is referred to Schippers (2017) for details. Note that the incipient motion is a function of an unknown friction coefficient (μ) for incipient motion due to sliding and an unknown location of the center of rotation (c/r) for incipient motion due to rotation. c is detailed below and r is the radius of the SOA. The incipient motion is determined for

$$F_{cr}(\mu) \leq F \quad \text{or} \quad M_{cr}(c/r) < M \tag{10}$$

Here, F is the force, the sub-index cr refers to critical conditions and M is the overturning moment. This means that the force or overturning moment is precisely reached, thus the incipient motion predicted in this work is more to be considered as rocking due to limited duration of the critical loading.

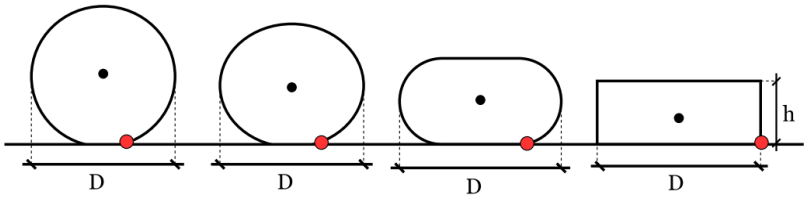

Figure 6: Examples of the transition between a circular and a rectangular cross section. Black dot: Centre of gravity. Red dot: Point of rotation.

One of the fundamental uncertainties related to the prediction of incipient motion (and actual transport) of SOAs is the shape uncertainty (Figure 6). Assuming that the SOA is perfectly circular, homogenous and lies on top of the plane bed, there is no restoring force against rotation. However, it was observed in the laboratory that there were indeed irregularities for the 'circular' SOAs given their creation process (hand-molding). Consequently, in order to quantify the sensitivity to shape a factor c/r is introduced in the stability analysis, where c is the horizontal distance from the center of gravity to the point of rotation. This parameter is a bulk representative of any deviation from a perfect circular cross section.

4.3 Critical Mobility Number

The critical mobility number is evaluated for the condition of a SOA lying on top of a flat bed. The results are depicted in Figure 7 for three values of c/r and four values of the friction coefficient. Furthermore, 6 data points from the experimental campaign described in Section 4.1 are included.

The incipient motion of a circular SOA is much more likely due to rotation than due to sliding. A large shape correction (c/r) is required for Ψ_{cr} to be smaller for sliding than for rotation. This hints at a direct consequence of the uncertainties related to the shape of SOAs in the field. Nonetheless, the measured critical mobility numbers are within the order of magnitude of the predictions by the numerical model.

The numerical predictions allows for an investigation of the effect of burial on the incipient motion of SOAs including the restoring force from the sand in the case of sliding. An example for a single diameter (0.1 m) and a single wave period (4.0 s) is depicted in Figure 8. The main observation for this parameter set

is that rotation is the most likely cause of incipient motion for $-0.05 < e/D$, while sliding is the more likely mechanisms for larger degrees of burial. Furthermore, it is seen that Ψ_{cr} becomes independent of c/r for $e/D < -0.15$, where the SOA rotates about the intersection point with the sand bed rather than the displaced point of rotation. This happens, because the distance to the intersection point exceeds c/r.

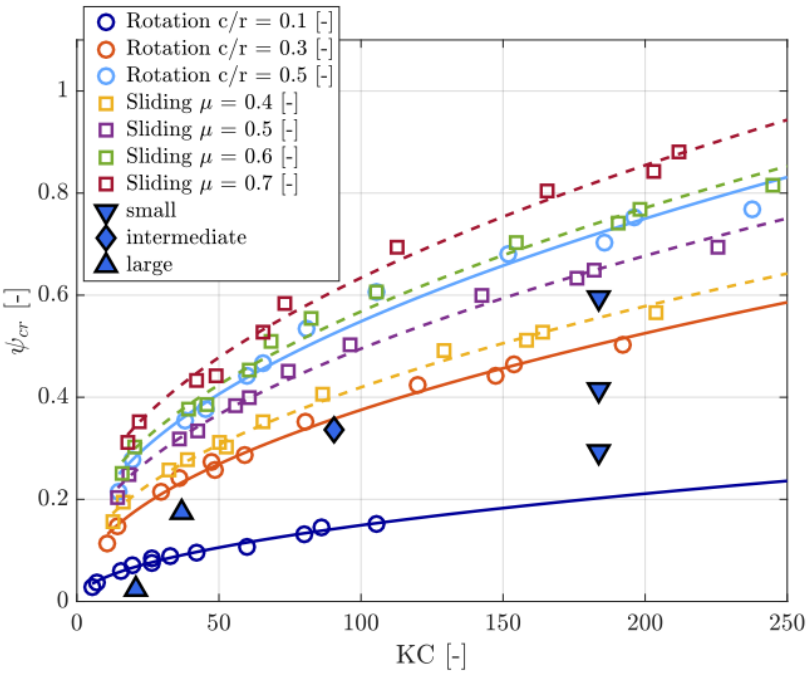

Figure 7: The critical mobility number for SOA in 2DV. Dashed lines related to incipient motion due to sliding and full lines to incipient motion due to rotation. $e/D = 0$. Open symbols are from numerical model and filled symbols are from laboratory observations.

The rapid increase in the critical mobility number for rotation with an increase in burial is due to the resulting horizontal force acts approximately at the half-height of the SOA irrespectively of the degree of burial (when the pressure field in the sand is accounted for). As a consequence, the contribution to the overturning moment from the horizontal force decreases linearly with an increase in burial. The results presented in this section are not sensitive to the actual density used in the calculations, since the density is a common factor in Eq. 10 (see Schippers, 2017, figure 6.10).

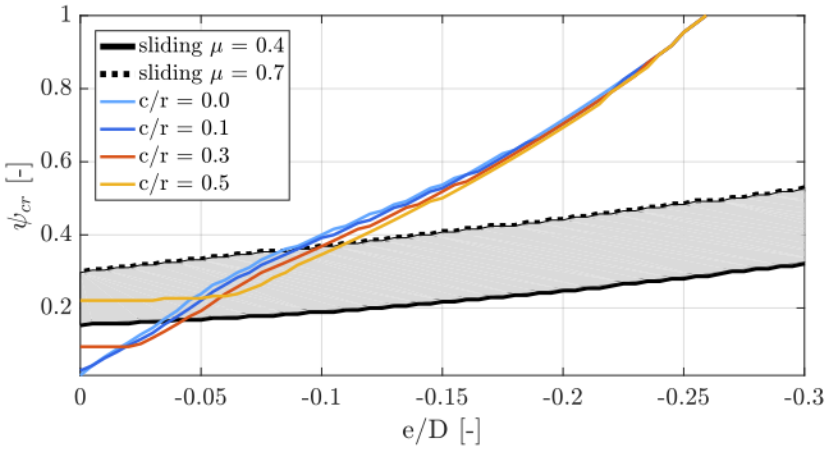

Figure 8: The critical mobility number as a function of the burial of the SOA. The shaded area shows range of critical mobility numbers for sliding and lines shows critical mobility numbers due to rotation.

4.3.1 Quantification of 3D effects

Two 3D simulations were performed with a period of $T = 8$ s and $u_m = 0.6$ m/s to investigate the effect of the 2DV simulation on the critical mobility number. In the first simulation, the SOA was modeled as a pipeline with a width of 0.5 m (relatively similar to the 2D approximation), while in the second simulation the SOA is a sphere. In both cases the diameter is 0.1 m and the SOAs are buried by 15%. The number of computational cells was approximately 2.3 million in both simulations. The non-dimensional force is defined as follows for the two objects (identical scaling for drag and lift forces):

$$F_{nondim,\,pipe} = \frac{2F}{\rho L D u_m^2} \quad \text{and} \quad F_{nondim,\,sphere} = \frac{8F}{\rho \pi D^2 u_m^2} \tag{11}$$

Here, L is the length of the pipe. The variation in the drag and lift force is depicted in Figure 9. In Section 1, the deviation of the experienced force from the one prediction by the Morison equation was discussed. This discrepancy is qualitatively seen in Figure 9, where the lift force has a large peak for the pipeline around $t/T = 3.55$ (maximum acceleration of the free stream). The peak in the lift force is observed for maximum free stream velocity for the sphere ($t/T = 3.75$). The Morison equation (Eq. 9) cannot capture the large acceleration-dominated lift force. The explanation for the large discrepancy between the assumed and actual loading of the pipeline is that the lee-wake vortex formed during one half-period is washed over the cylinder during flow reversal (large acceleration). The vortex is associated with a local negative pressure, which exerts a lift force on the pipeline. Unfortunately, it was observed too late in the process to adjust the data processing presented in this work.

In this work, the SOAs are modeled as pipelines, why the peak in the lift force is included (upper panel in Figure 9). Schippers (2017) found that the use of the 2DV approach over-predicted the critical mobility number by a factor of 1.5-2.0 for $KC < 100$. However, ignoring the force due to the sweeping vortex, the fitting to the Morison equation captured the remainder of the time variation well. The comparison in Figure 9 shows that a spherical object is much less sensitive to sweeping vortices, so the present analysis is a first and useful step in understanding the incipient motion of SOAs.

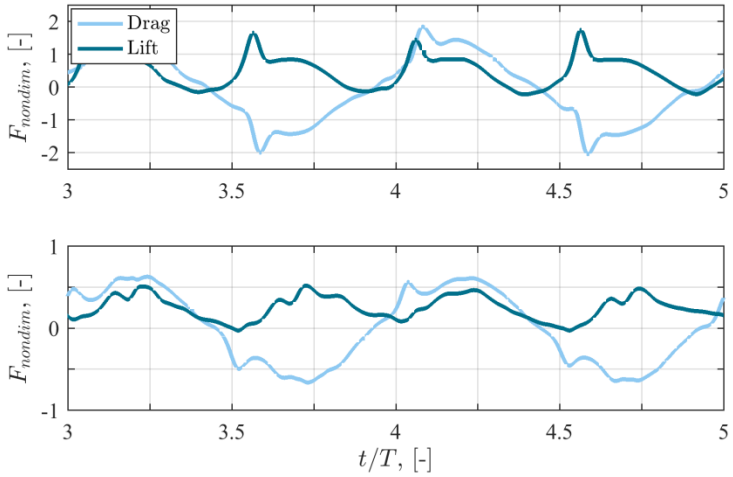

Figure 9: Comparison of the non-dimensional forces on a pipeline (upper panel) and a sphere (lower panel) for $KC = 48$.

5. Discussion and Conclusion

5.1 Discussion

Some of the uncertainties in the incipient motion of SOAs have already been mentioned above, namely the uncertainty related to the dimensions and shape of the SOA and the friction between the sand and the SOA. These factors themselves introduce a probability space for the likelihood of transport of SOAs. In addition to this, the results in Figure 9 show that the non-dimensional force differs by a factor of 2.0 between the pipeline and the spherical object, while the average weight per 'length' only differs by a factor of 1.5. This

suggests that spherical objects are more robust towards sliding than suggested from 2DV simulations.

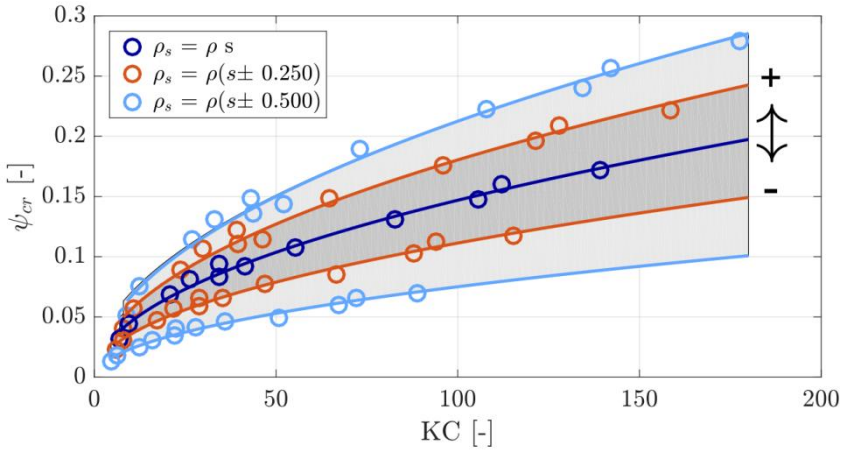

Figure 10: The uncertainty related to uncertainties in the density of the SOA. The mean is evaluated for $\rho_s = 2000$ kg/m^3.

An additional uncertainty is the actual density of the SOAs in the field. Density does not normally exhibit a wide variation for most non-cohesive nearshore environments, which are commonly dominated by quartz sand. If a representative density of 2000 kg/m3 is assumed in the modeling of SOAs then any deviation from this value directly influences the critical mobility number. This is illustrated in Figure 10, where the density is varied between 1500-2500 kg/m3 and the result is uncertainties of up to 40% with respect to the critical mobility number. As the mobility number is independent of the actual density, the variability in Figure 10 relates exclusively to mismatch between assumed densities and actual densities.

Furthermore, the sand surrounding SOAs will be mobilized prior to the incipient motion of SOAs (see Schippers, 2017). This means that local scour around the individual SOAs will take place and the SOAs will interact with bed forms such as ripples. The local scouring might be the mechanism responsible for self-burial of SOAs in a similar fashion to the processes studies for a single spherical object by Dixen et al. (2013). It would also be worthwhile to evaluate the magnitude of the hydraulic gradients in the sand bed, since large hydraulic gradient could potentially facilitate the sinking of SOAs.

In summary, the large number of uncertainties related not only to the numerical predictions, but also the actual conditions in the field (Dalyander et al., 2015a) suggest that a probabilistic modeling approach may be the preferred method to capture the incipient motion (and subsequent transport) of SOAs. Therefore, the risk of a new re-oiling incident becomes a function of the probability distribution of incipient motion of SOAs under specific hydrodynamic forcing.

5.2 Conclusion

In this work a newly developed model for the flow around a partly buried object was presented. A two-dimensional version of the numerical model was validated against existing theoretical and experimental data for wave-induced forces on pipelines. Comparison between force coefficients derived from fitting the simulated force to the Morison equations and theoretical and experimental data (based on an identical data treatment) shows a good comparison. The work also highlighted that the Morison equation is not well-suited for the description of forces on objects in 2DV (such as pipelines), when the objects are placed on the seabed. A 3D simulation suggests these effects are less important for spherical objects.

The work highlighted a number of uncertainties for the prediction of incipient motion of SOAs. The uncertainties relate to a large extent to the forcing mechanism and consequently the natural variability of SOA properties. The uncertainties are: shape of the SOA, dimensions of the SOA, density of the SOA, friction between SOA and seabed, local scouring, and influence of bed forms. The direct consequence is that it is unlikely that the modeling of incipient motion (and subsequent transport) of SOAs – in a practical

engineering model – is realistic in a deterministic fashion. The present CFD model, however, is useful in providing insights into the impact of the natural variability of SOAs.

Acknowledgements
Funding for this research was provided by USGS and through Deltares Strategic Research in the "Hydro- and morphodynamics during extreme events" program (1230002). Any use of trade, firm, or product names is for descriptive purposes only and does not imply endorsement by the U.S. Government.

References

An, H., Cheng, L. and Zhao, M. (2011). Numerical simulation of a partially buried pipeline in a permeable seabed subject to combined oscillatory flow and steady current. *Ocean Engineering*, **38**, 1225-1236.

Bryndum, M.B., Jacobsen, V. and Tsahalis, D.T. (1992). Hydrodynamic forces on pipelines: Model tests. *Journal of Offshore Mechanics and Arctic Engineering*, **114**, 231-241.

Dalyander, P.S., Long, J.W., Plant, N.G. and Thomson, D.M. (2014). Assessing mobility and redistribution patterns of sand and oil agglomerates in the surf zone. *Marine Pollution Bulletin*, **80**, 200-209.

Dalyander, P.S., Plant, N.G., Long, J.W. and McLaughlin, M. (2015a). Nearshore dynamics of artificial sand and oil agglomerates. *Marine Pollution Bulletin*, **96**, 344-355, http://doi.org/10.1016/j.marpolbul.2015.04.049.

Dalyander, P.S., Long, J.W., Plant, N.G, McLaughlin, Molly, and Mickey, R.C., 2015, Field Observations of Artificial Sand and Oil Agglomerates: U.S. Geological Survey Open-File Report 2015–1075, https://dx.doi.org/10.3133/ofr20151057.

Dixen, M., Sumer, B.M. and Fredsøe, J. (2013). Numerical and experimental investigation of flow and scour around a half-buried sphere. *Coastal Engineering*, **73**, 84-105.

Frank, D., Foster, D., Sou, I.M., and Calantoni, J. (2015). Incipient motion of surf zone sediments. *Journal of Geophysical Research: Oceans,* **120**(8): 5710-5734.

Jacobsen, V., Bryndum, M.B. and Tsahalis, D.T. (1988). Prediction of irregular wave forces on submarine pipelines. *Proceedings for Seventh International Conference on Offshore Mechanics and Arctic Engineering*, 23-32.

Jacobsen, V., Bryndum, M.B. and Bonde, C. (1989). Fluid loads on pipelines: Sheltered or sliding. *Offshore Technology Conference*, OTC 6056, 133-146.

Jensen, B.L., Sumer, B.M. and Fredsøe, J. (1989). Turbulent oscillatory boundary layers at high Reynolds numbers. *Journal of Fluid Mechanics*, **206**, 265-297.

Schippers, M.M.A. (2017). *Incipient motion of sand and oil agglomerates – A numerical study on the mobility of particles under wave-induced forcing*. Master thesis. Delft University of Technology.

Sumer, B.M and Fredsøe, J. (1999). *Hydrodynamics around cylindrical structures*. Advanced Series on Coastal Engineering, **12**, World Scientific, 1st edition.

Terrile, E., Reniers, A.J.H.M., Stive, M.J.F., Tromp, M. And Verhagen, H.J. (2006). Incipient motion of coarse particles under regular shoaling waves. *Coastal Engineering,* **53**(1): 81-92.

Van Gent, M.R.A. (1995). Porous flow through rubble mound material, *Journal of Waterway, Port, Coastal and Ocean Engineering – ASCE*, **121**(3), 176-181.

Weller, H.G., Tabor, G., Jasak, H. and Fureby, C. (1998). A tensorial approach to computational continuum mechanics using object oriented techniques. *Computers in Physics*, **12**(6), 620-631.

Wilcox, D.C. (2006). *Turbulence modeling for CFD*. DCW Industries, 3rd edition.

Yamamoto, T., Nath, J.H. and Slotta, L.S. (1974). Wave forces on cylinders near plane boundary. *Journal of the Waterways, Harbors and Coastal Engineering Division – ASCE*, **100**(4), 345-360